Supplement of Biogeosciences, 19, 1087–1109, 2022
https://doi.org/10.5194/bg-19-1087-2022-supplement

Biogeosciences
Open Access

Supplement of

A seamless ensemble-based reconstruction of surface ocean $p\mathrm{CO_2}$ and air–sea CO_2 fluxes over the global coastal and open oceans

Thi Tuyet Trang Chau et al.

Correspondence to: Thi Tuyet Trang Chau (trang.chau@lsce.ipsl.fr)

Table S1. Input fields for the CMEMS-LSCE-FFNN reconstruction of sea surface partial pressure of $\mathrm{CO_2}$ ($p\mathrm{CO_2}$) and air–sea $\mathrm{CO_2}$ fluxes ($fg\mathrm{CO_2}$) over the global ocean in 1985–2019.

Variables		Products	References
1	$\mathrm{CO_2}$ fugacity	SOCATv2020, 1985-2019 (https://www.socat.info/, https://doi.org/10.25921/4xkx-ss49, last access 16/6/2020)	Bakker et al. (2016)
2	Sea surface salinity (SSS)	CMEMS ARMOR3D L4, 1993-2019 (https://resources.marine.copernicus.eu/?option=com_csw&view=details&product_id=MULTIOBS_GLO_PHY_TSUV_3D_MYNRT_015_012)	Guinehut et al. (2012)
3	Sea surface height (SSH)		Mulet et al. (2012)
4	Sea surface temperature (SST)	CMEMS ARMOR3D L4, 1993-2019; OSTIA L4*, 1985-1992 (https://resources.marine.copernicus.eu/?option=com_csw&view=details&product_id=SST_GLO_SST_L4_REP_OBSERVATIONS_010_011)	Good et al. (2020)*
5	Mixed layer depth (MLD)	ECCO2, 1992-2019 (https://ecco.jpl.nasa.gov)	Menemenlis et al. (2008)
6	Chlorophyll (CHL)	GLOCOLOUR, 1998-2019 (https://www.globcolour.info/)	Maritorena et al. (2010)
7	$\mathrm{CO_2}$ mole fraction ($x\mathrm{CO_2}$)	CAMS $\mathrm{CO_2}$ atmospheric inversion, 1985-2019 (https://atmosphere.copernicus.eu/)	Chevallier et al. (2005, 2010) Chevallier (2013)
8	$p\mathrm{CO_2}$ climatology ($p\mathrm{CO_2^{clim}}$)	LDEO (https://www.ldeo.columbia.edu/res/pi/CO2/)	Takahashi et al. (2009)
9	6-hourly $10\mathrm{m}$ winds	ERA5, 1985-2019 (https://www.ecmwf.int/en/forecasts/datasets/reanalysis-datasets/era5)	Hersbach et al. (2020)
10	Total pressure		
11	Sea ice fraction (f_{ice})	CMEMS OSTIA L4, 1985-2019, (https://resources.marine.copernicus.eu/?option=com_csw&view=details&product_id=SST_GLO_SST_L4_REP_OBSERVATIONS_010_011, https://resources.marine.copernicus.eu/?option=com_csw&view=details&product_id=SST_GLO_SST_L4_NRT_OBSERVATIONS_010_001)	Good et al. (2020)

**For some data unavailable before 1998, climatologies based on all available data were used as predictors. Exceptionally, predictors for SSH before 1993 are climatologies plus a linear trend in order to retain the overall response to the global warming. MLD before 1992 was taken as the average MLD between 1992 and 1997.

Table S2. Skill scores of the CMEMS-LSCE-FFNN reconstruction for different RECCAP regions. Validation between the reconstructed $p\mathrm{CO_2}$ ($\mu\mathrm{atm}$), $fg\mathrm{CO_2}$ ($\mathrm{molC\,m^{-2}yr^{-1}}$), and the corresponding fields computed from the monthly gridded SOCATv2020 data over the full period $1985-2019$. Statistical metrics include Root Mean Square Deviation (RMSD) and coefficient of determination (r^2).

	Regions	Number of data		$\mathrm{RMSD}_{p\mathrm{CO_2}}$		$r^2_{p\mathrm{CO_2}}$		$\mathrm{RMSD}_{fg\mathrm{CO_2}}$		$r^2_{fg\mathrm{CO_2}}$	
		O	C	O	C	O	C	O	C	O	C
	Globe (G)	270228	31221	17.87	35.86	0.78	0.70	0.93	1.91	0.79	0.64
1	Arctic (Ar)	1170	449	33.01	30.65	0.61	0.44	1.11	0.93	0.70	0.77
2	Subpolar Atlantic (SpA)	24433	12249	23.68	30.35	0.76	0.79	1.35	1.66	0.69	0.75
3	Subpolar Pacific (SpP)	10840	3596	29.08	54.69	0.64	0.57	1.80	2.70	0.66	0.54
4	Subtropical Atlantic (StA)	50113	5205	15.24	34.74	0.76	0.51	0.77	2.39	0.77	0.37
5	Subtropical Pacific (StP)	67950	853	17.15	47.29	0.78	0.45	0.81	2.08	0.84	0.48
6	Equatorial Atlantic (EA)	11574	469	14.11	36.03	0.69	0.25	0.53	1.14	0.64	0.36
7	Equatorial Pacific (EP)	45590	221	16.68	27.17	0.80	0.41	0.57	0.84	0.81	0.38
8	South Atlantic (SA)	4577	562	14.09	37.98	0.77	0.46	0.71	2.00	0.78	0.42
9	South Pacific (SP)	17074	1181	11.50	14.38	0.76	0.60	0.56	0.71	0.79	0.62
10	Indian Ocean (IO)	7792	588	14.60	18.37	0.80	0.65	1.02	0.91	0.78	0.68
11	Southern Ocean (SO)	29115	5848	19.18	35.73	0.62	0.65	1.24	1.64	0.53	0.64

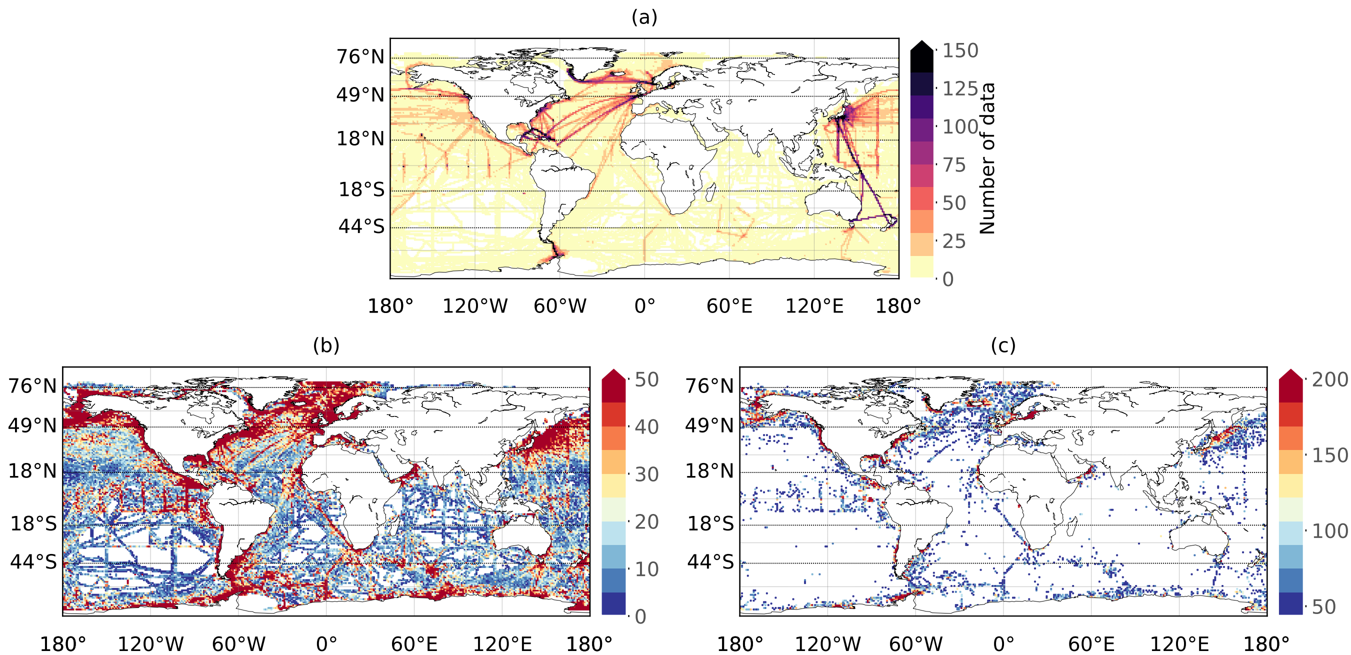

Figure S1. (a) Spatial distribution of monthly gridded SOCATv2020 data. (b,c) Maximal variability of $p\mathrm{CO}_2$ individual data within a $1^\circ \times 1^\circ$-grid box (μatm), i.e. $\max_t\{p\mathrm{CO}_{2,tij}^{\max} - p\mathrm{CO}_{2,tij}^{\min}\}$, where t and ij indicate time and space indices. $p\mathrm{CO}_{2,tij}^{\max}$ and $p\mathrm{CO}_{2,tij}^{\min}$ were converted from the corresponding values of CO_2 fugacity observations in the monthly gridded SOCATv2020 database. Fig. S1c shows the distribution of the variability larger than the 80%-quantile.

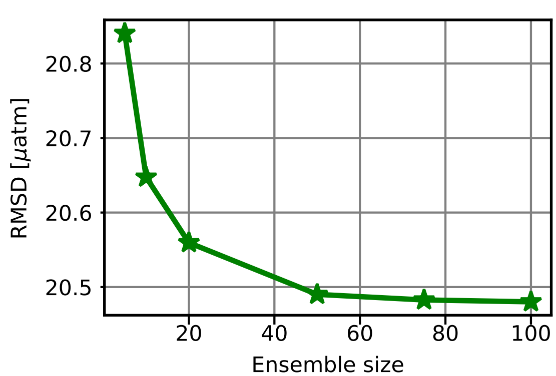

Figure S2. RMSD between a best estimate (ensemble mean) and SOCAT data of ocean surface $p\mathrm{CO}_2$ with respect to the ensemble size in $\{5,\ 10,\ 20,\ 50,\ 75,\ 100\}$.

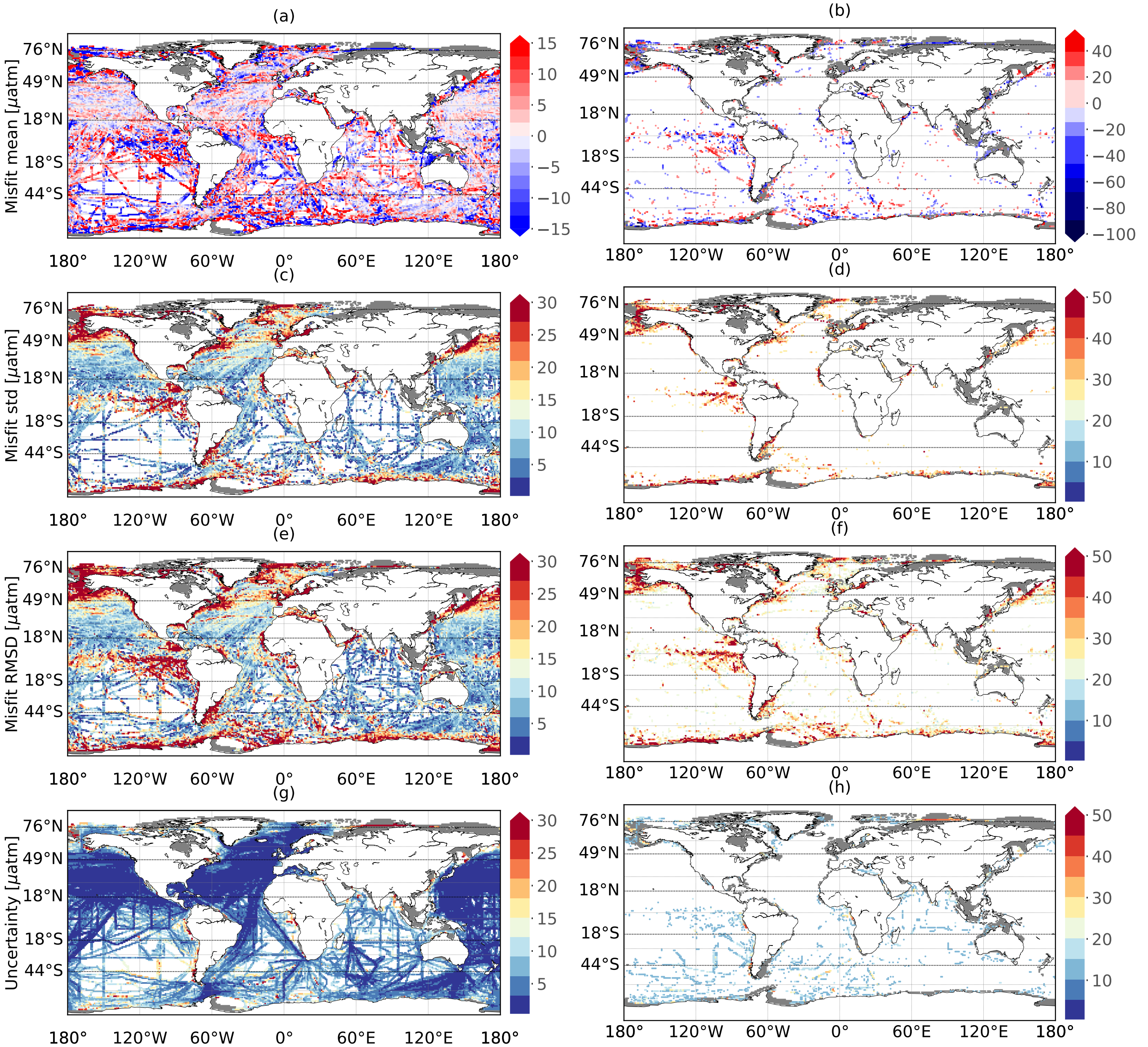

Figure S3. Temporal mean (a,b), standard deviation (c,d), and RMSD (e,f) of model-minus-data misfits between the reconstructed $p\mathrm{CO}_2$ and SOCAT data; and model uncertainty (g,h), i.e. ensemble standard deviation of temporal mean estimates at SOCAT grid boxes. The right column plots show statistics falling out of the 90% quantile range for (b), or larger than the 90%-quantile for (d,f,h).

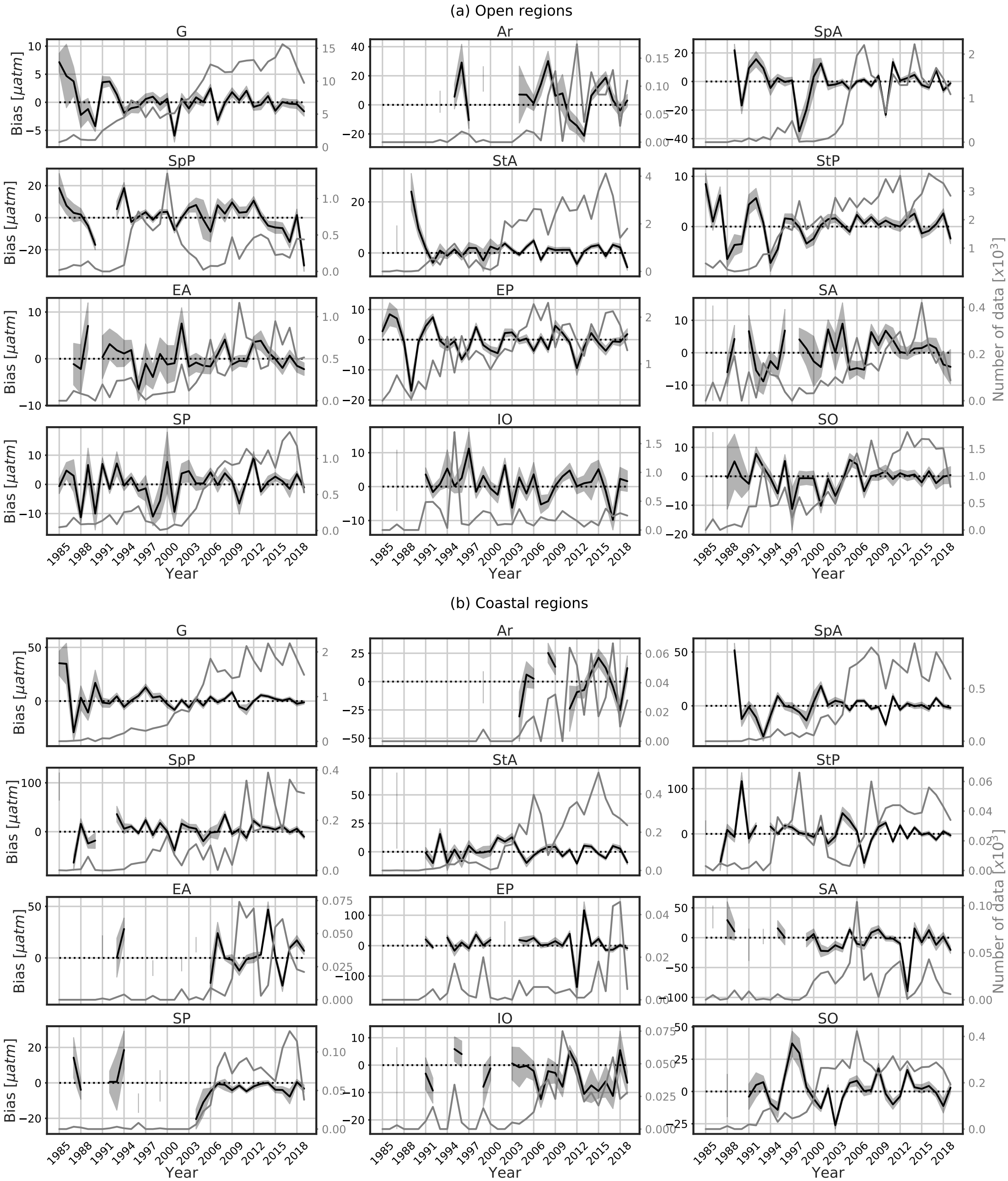

Figure S4. Time series of the yearly mean bias between the reconstructed $p\mathrm{CO}_2$ data and SOCATv2020 data over the open ocean and coastal area (black curve) and of the total number of monthly gridded data used in the FFNN model construction (light grey curve). The grey area represents the 1σ-envelop of the errors derived from the 100-member ensemble.

Table S3. Names, locations, and time length of moored time series of $p\mathrm{CO_2}$ observations (Sutton et al., 2019) sampled over the open ocean (O) and coastal ocean (C).

	Stations		Coordinates	Time span
	Abbreviations	Names	(Latitude, Longitude)	
(O)	1. ALAWAI	Ala Wai Water Quality Buoy Pacific island	21.3°N, 157.9°W	6/2008–12/2013
	2. BOBOA	Bay of Bengal Ocean Indian Ocean	15.0°N, 90.0°E	11/2013–12/2016
	3. BTM	Bermuda Testbed Mooring	31.5°N, 64.2°W	10/2005–12/2006
	4. CCE1	California Current Ecosystem 1	33.5°N, 122.5°W	11/2008–12/2013
	5. CHUUK	Chuuk Lagoon Ocean Acidification Mooring	7.5°N, 151.9°E	11/2011–12/2014
	6. CRESCENTREEF	Crescent Reef Bermuda Buoy	32.4°N, 64.8°W	11/2010–12/2014
	7. CRIMP2	Coral Reef Instrumented Monitoring Platform 2	21.5°N, 157.8°W	6/2008–12/2014
	8. HOGREEF	Hog Reef Bermuda Buoy	32.5°N, 64.8°W	12/2010–12/2014
	9. KANEOHE	Kaneohe Bay Ocean Acidification Offshore Observatory	21.5°N, 157.8°W	9/2011–5/2015
	10. KEO	Kuroshio Extension Observatory	32.3°N, 144.6°E	9/2007–12/2014
	11. KILONALU	Kilo Nalu Water Quality Buoy at South Shore Oahu	21.3°N, 157.9°W	8/2008–12/2016
	12. NH10	Newport Hydrographic Line Station 10 Ocean Acidification Mooring	44.9°N, 124.8°W	4/2014–12/2014
	13. PAPA	Ocean Station Papa	50.1°N, 144.8°W	6/2007–12/2014
	14. SOFS	Southern Ocean Flux Station	46.8°S, 142.0°E	11/2011–9/2012
	15. STRATUS	Stratus	19.7°S, 85.6°W	10/2006–12/2014
	16. TAO110W	National Data Buoy Center (NDBC) Tropical Atmosphere Ocean	0.0°N, 110.0°W	9/2009–12/2016
	17. TAO125W	NDBC Tropical Atmosphere Ocean	0.0°N, 125.0°W	5/2004–12/2016
	18. TAO140W	NDBC Tropical Atmosphere Ocean	0.0°N, 140.0°W	5/2004–4/2012
	19. TAO155W	NDBC Tropical Atmosphere Ocean	0.0°N, 155.0°W	1/2010–12/2013
	20. TAO165E	NDBC Tropical Atmosphere Ocean	0.0°N, 165.0°E	2/2010–11/2011
	21. TAO170W	NDBC Tropical Atmosphere Ocean	0.0°N, 170.0°W	7/2005–12/2011
	22 TAO8S165E	NDBC Tropical Atmosphere Ocean	8.0°S, 165.0°E	6/2009–12/2010
	23. WHOTS	Woods Hole Oceanographic Institution Hawaii Ocean Time-series Station	22.7°N, 158.0°W	12/2004–12/2014
(C)	1. CAPEELIZABETH	NDBC Buoy 46041 in Olympic Coast National Marine Sanctuary (NMS)	47.4°N, 124.7°W	6/2006–12/2014
	2. CCE2	California Current Ecosystem 2	34.3°N, 120.8°W	1/2010–12/2014
	3. CHABA	Chá bˇa Buoy in the Northwest Enhanced Moored Observatory and Olympic Coast NMS	48.0°N, 126.0°W	7/2010–11/2015
	4. CHEECAROCKS	Cheeca Rocks Ocean Acidification Mooring in Florida Keys National Marine Sanctuary	24.9°N, 80.6°W	12/2011–12/2015
	5. COASTALMS	Central Gulf of Mexico Ocean Observing System Station 01	30.0°N, 88.6°W	5/2009–5/2014
	6.GAKOA	Gulf of Alaska Ocean Acidification Mooring	59.9°N, 149.4°W	5/2011–12/2016
	7. GRAYSREEF	NDBC Buoy 41008 in Gray's Reef National Marine Sanctuary	31.4°N, 80.9°W	7/2006–12/2014
	8. GULFOFMAINE	Coastal Western Gulf of Maine Mooring	43.0°N, 70.5°W	7/2006–12/2014
	9. ICELAND	North Atlantic Ocean Acidification Mooring	68.0°N, 12.7°W	8/2013–11/2014
	10. KODIAK	Kodiak Alaska Ocean Acidification Mooring	57.7°N, 152.3°W	3/2013–12/2015
	11. LAPARGUERA	La Parguera Ocean Acidification Mooring	18.0°N, 67.1°W	1/2009–12/2016
	12. M2	Southeastern Bering Sea Mooring Site 2	56.5°N, 164.0°W	5/2013–9/2015
	13. SEAK	Southeast Alaska Ocean Acidification Mooring	56.3°N, 134.7°W	3/2013–12/2015

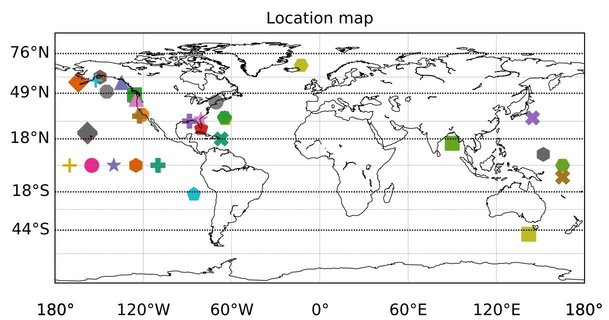

Figure S5. Location map of in situ measurements of ocean surface $p\mathrm{CO}_2$ (Sutton et al., 2019).

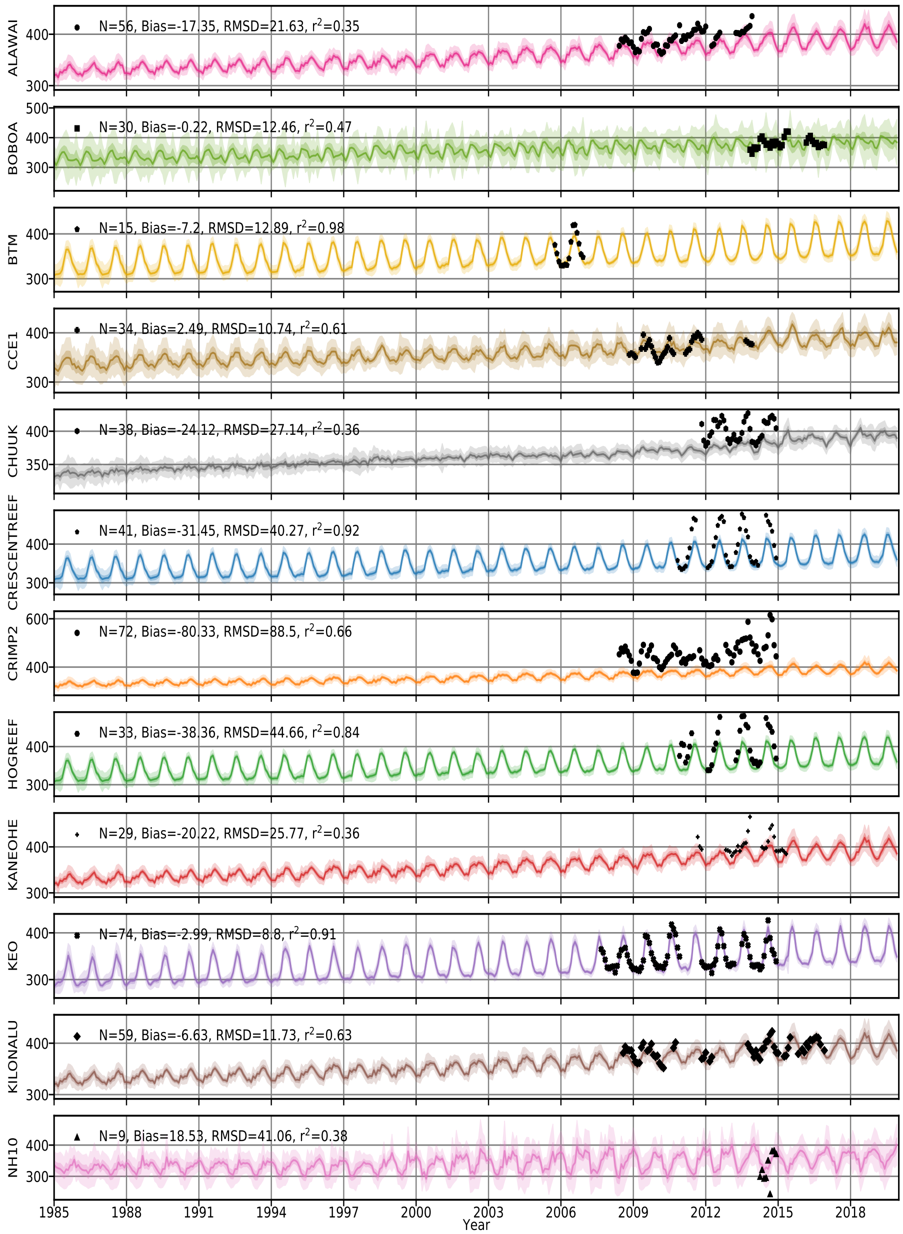

Figure S6. Time series of open ocean surface $p\mathrm{CO}_2$ at different stations - part 1 (see station locations in Fig. S5 and Table S3). Evaluation data are monthly averages of measurements at each station (Sutton et al., 2019). The ensemble mean μ_{ensemble} and ensemble spread $\sigma_{\mathrm{ensemble}}$ (Eq. 2) are computed from reconstructed data at the four nearest neighbors of that location. Number of grid boxes with observations N, model bias μ_{misfit} (Eq. 3), RMSD (Eq. 4), and model–data correlation r^2 have been computed on these monthly interpolated data. In each subplot, dots stand for observation–based data and the coloured line with shaded areas stand for the mean and uncertainty envelops computed from the CMEMS-LSCE-FFNN 100-member ensemble (dark: 68% confidence interval, i.e. $\mu_{\mathrm{ensemble}} \pm \sigma_{\mathrm{ensemble}}$; light: 99% confidence interval, i.e. $\mu_{\mathrm{ensemble}} \pm 3\sigma_{\mathrm{ensemble}}$).

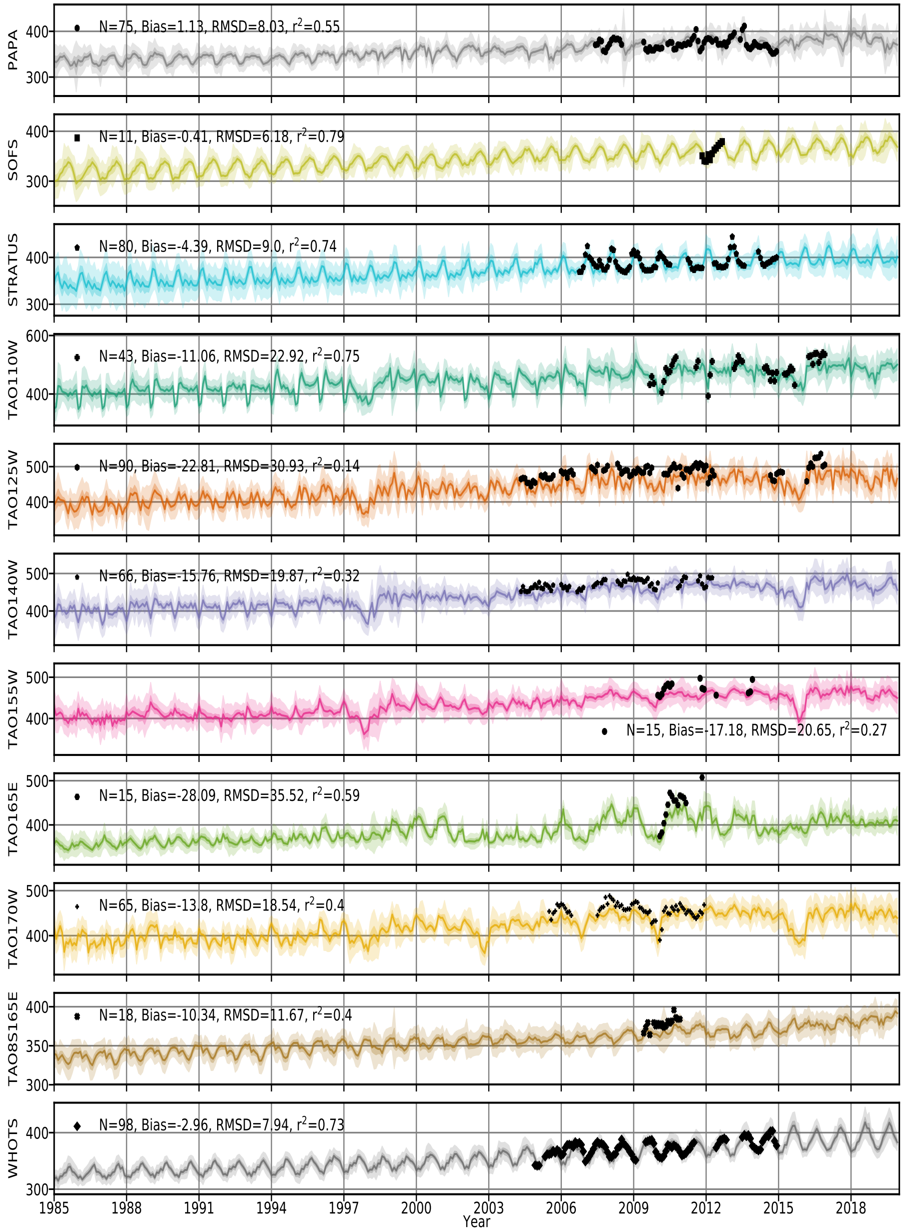

Figure S7. Time series of open ocean surface $p\mathrm{CO}_2$ at different stations - part 2 (see station locations in Fig. S5 and Table S3). Evaluation data are monthly averages of measurements at each station (Sutton et al., 2019). The ensemble mean μ_{ensemble} and ensemble spread $\sigma_{\mathrm{ensemble}}$ (Eq. 2) are computed from reconstructed data at the four nearest neighbors of that location. Number of grid boxes with observations N, model bias μ_{misfit} (Eq. 3), RMSD (Eq. 4), and model–data correlation r^2 have been computed on these monthly interpolated data. In each subplot, dots stand for observation–based data and the coloured line with shaded areas stand for the mean and uncertainty envelops computed from the CMEMS-LSCE-FFNN 100-member ensemble (dark: 68% confidence interval, i.e. $\mu_{\mathrm{ensemble}} \pm \sigma_{\mathrm{ensemble}}$; light: 99% confidence interval, i.e. $\mu_{\mathrm{ensemble}} \pm 3\sigma_{\mathrm{ensemble}}$).

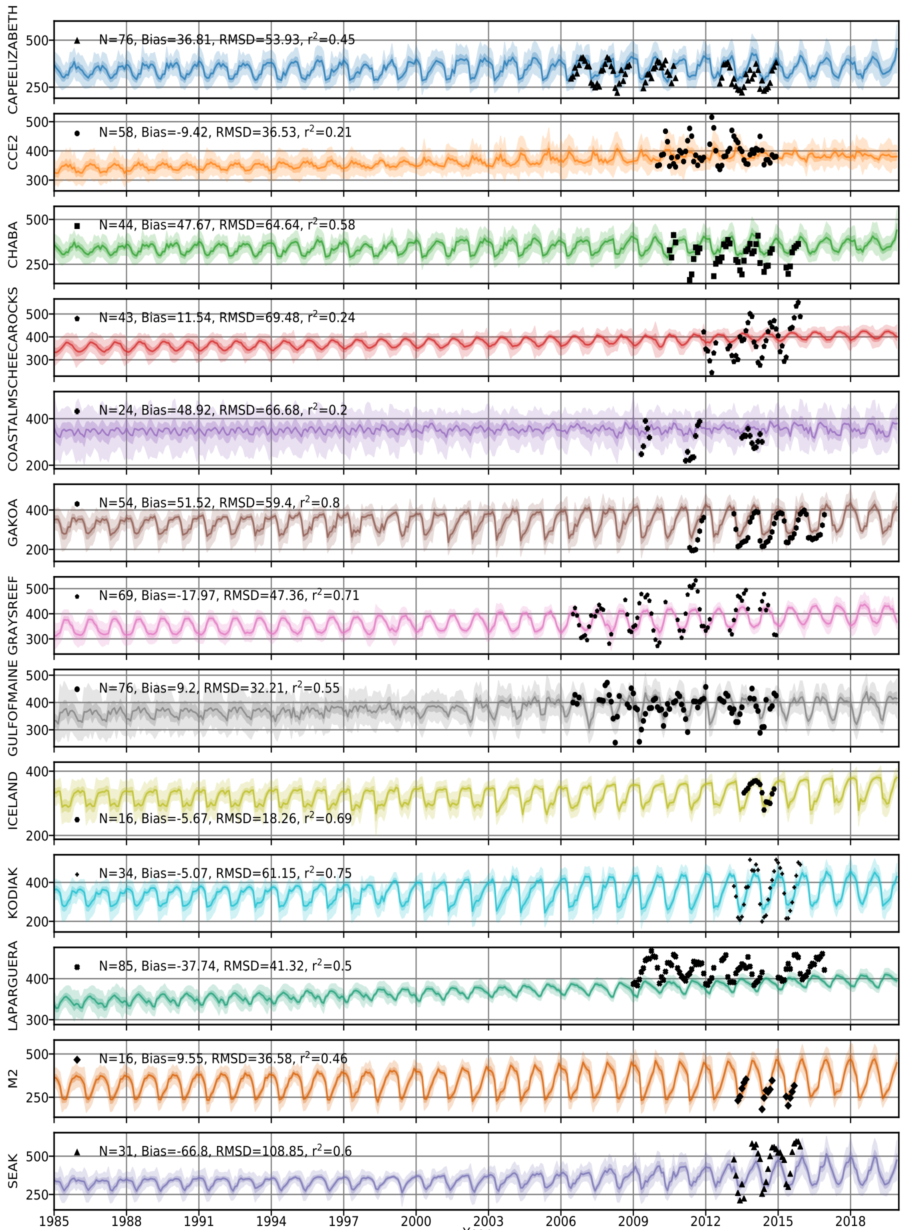

Figure S8. Time series of coastal ocean surface $p\mathrm{CO}_2$ at different stations (see station locations in Fig. S5). Evaluation data are monthly averages of measurements at each station (Sutton et al., 2019). The ensemble mean μ_{ensemble} and ensemble spread $\sigma_{\mathrm{ensemble}}$ (Eq. 2) are computed from reconstructed data at the four nearest neighbors of that location. Number of grid boxes with observations N, model bias μ_{misfit} (Eq. 3), RMSD (Eq. 4), and model–data correlation r^2 have been computed on these monthly interpolated data. In each subplot, dots stand for observation–based data and the coloured line with shaded areas stand for the mean and uncertainty envelops computed from the CMEMS-LSCE-FFNN 100-member ensemble (dark: 68% confidence interval, i.e. $\mu_{\mathrm{ensemble}} \pm \sigma_{\mathrm{ensemble}}$; light: 99% confidence interval, i.e. $\mu_{\mathrm{ensemble}} \pm 3\sigma_{\mathrm{ensemble}}$).

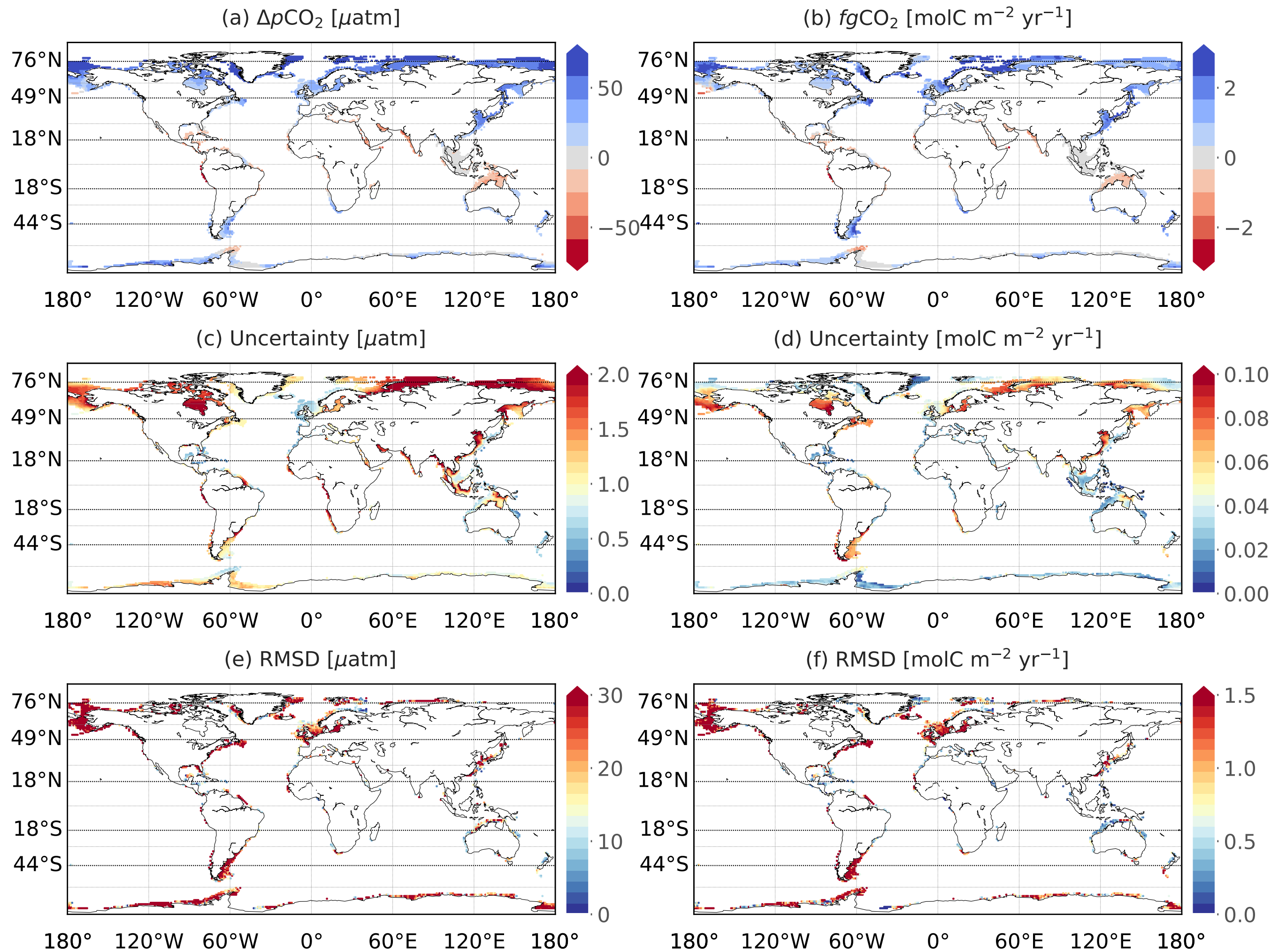

Figure S9. Climatological mean (top) and uncertainty (middle) of air-sea $p\mathrm{CO_2}$ difference (a, c) and of $\mathrm{CO_2}$ fluxes (b, d) over the coastal ocean for 1985-2019. Uncertainty is computed as standard deviation of the 100-member CMEMS-LSCE-FFNN model outputs of sea surface $p\mathrm{CO_2}$ and air-sea $\mathrm{CO_2}$ fluxes. The bottom plots (e, f) show RMSDs between the SOCAT data (or data-based estimates of fluxes for (f)) and the mean CMEMS-LSCE-FFNN model outputs.

References

Bakker, D. C. E., Pfeil, B., Landa, C. S., Metzl, N., O'Brien, K. M., Olsen, A., Smith, K., Cosca, C., Harasawa, S., Jones, S. D., Nakaoka, S., Nojiri, Y., Schuster, U., Steinhoff, T., Sweeney, C., Takahashi, T., Tilbrook, B., Wada, C., Wanninkhof, R., Alin, S. R., Balestrini, C. F., Barbero, L., Bates, N. R., Bianchi, A. A., Bonou, F., Boutin, J., Bozec, Y., Burger, E. F., Cai, W.-J., Castle, R. D., Chen, L., Chierici, M., Currie, K., Evans, W., Featherstone, C., Feely, R. A., Fransson, A., Goyet, C., Greenwood, N., Gregor, L., Hankin, S., Hardman-Mountford, N. J., Harlay, J., Hauck, J., Hoppema, M., Humphreys, M. P., Hunt, C. W., Huss, B., Ibánhez, J. S. P., Johannessen, T., Keeling, R., Kitidis, V., Körtzinger, A., Kozyr, A., Krasakopoulou, E., Kuwata, A., Landschützer, P., Lauvset, S. K., Lefèvre, N., Lo Monaco, C., Manke, A., Mathis, J. T., Merlivat, L., Millero, F. J., Monteiro, P. M. S., Munro, D. R., Murata, A., Newberger, T., Omar, A. M., Ono, T., Paterson, K., Pearce, D., Pierrot, D., Robbins, L. L., Saito, S., Salisbury, J., Schlitzer, R., Schneider, B., Schweitzer, R., Sieger, R., Skjelvan, I., Sullivan, K. F., Sutherland, S. C., Sutton, A. J., Tadokoro, K., Telszewski, M., Tuma, M., van Heuven, S. M. A. C., Vandemark, D., Ward, B., Watson, A. J., and Xu, S.: A multi-decade record of high-quality fCO_2 data in version 3 of the Surface Ocean CO_2 Atlas (SOCAT), Earth Syst. Sci. Data, 8, 383–413, https://doi.org/10.5194/essd-8-383-2016, 2016.

Chevallier, F.: On the parallelization of atmospheric inversions of CO_2 surface fluxes within a variational framework, Geosci. Model Dev., 6, 783–790, https://doi.org/10.5194/gmd-6-783-2013, 2013.

Chevallier, F., Fisher, M., Peylin, P., Serrar, S., Bousquet, P., Bréon, F.-M., Chédin, A., and Ciais, P.: Inferring CO_2 sources and sinks from satellite observations: Method and application to TOVS data, J. Geophys. Res. Atmos., 110, https://doi.org/https://doi.org/10.1029/2005JD006390, 2005.

Chevallier, F., Ciais, P., Conway, T. J., Aalto, T., Anderson, B. E., Bousquet, P., Brunke, E. G., Ciattaglia, L., Esaki, Y., Fröhlich, M., Gomez, A., Gomez-Pelaez, A. J., Haszpra, L., Krummel, P. B., Langenfelds, R. L., Leuenberger, M., Machida, T., Maignan, F., Matsueda, H., Morguí, J. A., Mukai, H., Nakazawa, T., Peylin, P., Ramonet, M., Rivier, L., Sawa, Y., Schmidt, M., Steele, L. P., Vay, S. A., Vermeulen, A. T., Wofsy, S., and Worthy, D.: CO_2 surface fluxes at grid point scale estimated from a global 21 year reanalysis of atmospheric measurements, J. Geophys. Res. Atmos., 115, https://doi.org/https://doi.org/10.1029/2010JD013887, 2010.

Good, S., Fiedler, E., Mao, C., Martin, M. J., Maycock, A., Reid, R., Roberts-Jones, J., Searle, T., Waters, J., While, J., and Worsfold, M.: The current configuration of the OSTIA system for Operational Production of Foundation Sea Surface Temperature and Ice Concentration Analyses, Remote Sens., 12, https://www.mdpi.com/2072-4292/12/4/720, 2020.

Guinehut, S., Dhomps, A.-L., Larnicol, G., and Le Traon, P.-Y.: High resolution 3-D temperature and salinity fields derived from in situ and satellite observations, Ocean Sci., 8, 845–857, https://doi.org/10.5194/os-8-845-2012, 2012.

Hersbach, H., Bell, B., Berrisford, P., Hirahara, S., Horányi, A., Muñoz-Sabater, J., Nicolas, J., Peubey, C., Radu, R., Schepers, D., Simmons, A., Soci, C., Abdalla, S., Abellan, X., Balsamo, G., Bechtold, P., Biavati, G., Bidlot, J., Bonavita, M., De Chiara, G., Dahlgren, P., Dee, D., Diamantakis, M., Dragani, R., Flemming, J., Forbes, R., Fuentes, M., Geer, A., Haimberger, L., Healy, S., Hogan, R. J., Hólm, E., Janisková, M., Keeley, S., Laloyaux, P., Lopez, P., Lupu, C., Radnoti, G., de Rosnay, P., Rozum, I., Vamborg, F., Villaume, S., and Thépaut, J.-N.: The ERA5 global reanalysis, Q. J. R. Meteorol. Soc., 146, 1999–2049, https://doi.org/https://doi.org/10.1002/qj.3803, 2020.

Maritorena, S., d'Andon, O. H. F., Mangin, A., and Siegel, D. A.: Merged satellite ocean color data products using a bio-optical model: Characteristics, benefits and issues, Remote Sens. Environ., 114, 1791–1804, https://doi.org/https://doi.org/10.1016/j.rse.2010.04.002, 2010.

Menemenlis, D., Campin, J., Heimbach, P., Hill, C., Lee, T., Nguyen, A., Schodlok, M., and Zhang, H.: ECCO2: High resolution global ocean and sea ice data synthesis, OS31C-1292, 2008.

Mulet, S., Rio, M.-H., Mignot, A., Guinehut, S., and Morrow, R.: A new estimate of the global 3D geostrophic ocean circulation based on satellite data and in-situ measurements, Deep Sea Res. 2 Top. Stud. Oceanogr., 77-80, 70–81, https://doi.org/https://doi.org/10.1016/j.dsr2.2012.04.012, 2012.

Sutton, A. J., Feely, R. A., Maenner-Jones, S., Musielwicz, S., Osborne, J., Dietrich, C., Monacci, N., Cross, J., Bott, R., Kozyr, A., et al.: Autonomous seawater pCO$_2$ and pH time series from 40 surface buoys and the emergence of anthropogenic trends, Earth Syst. Sci. Data, 11, 421–439, 2019.

Takahashi, T., Sutherland, S. C., Wanninkhof, R., Sweeney, C., Feely, R. A., Chipman, D. W., Hales, B., Friederich, G., Chavez, F., Sabine, C., Watson, A., Bakker, D. C., Schuster, U., Metzl, N., Yoshikawa-Inoue, H., Ishii, M., Midorikawa, T., Nojiri, Y., Körtzinger, A., Steinhoff, T., Hoppema, M., Olafsson, J., Arnarson, T. S., Tilbrook, B., Johannessen, T., Olsen, A., Bellerby, R., Wong, C., Delille, B., Bates, N., and de Baar, H. J.: Climatological mean and decadal change in surface ocean pCO$_2$, and net sea–air CO$_2$ flux over the global oceans, Deep Sea Res. 2 Top. Stud. Oceanogr., 56, 554–577, https://doi.org/https://doi.org/10.1016/j.dsr2.2008.12.009, 2009.